Detailed Analysis of the Thrust Oscillations in Reduced Scale Solid Rocket Motors

F. Chedevergne* and G. Casalis†

ONERA, 2 av. Edouard Belin, BP 4025, 31 055 Toulouse Cedex, FRANCE

Solid rocket motors exhibit undesirable thrust oscillations at the end of their firing. These oscillations are linked to inflow pressure fluctuations induced by flow instabilities. A biglobal linear stability analysis has confirmed the role of the parietal vortex shedding in this phenomenon. This approach, based on a small perturbation technique, leads to a global understanding of the thrust oscillations. Using these results, the present paper provides a detailed analysis thanks to comparisons with reduced scale motors measurements.

Nomenclature

ω_i	temporal growth rate
ω_r	circular frequency
θ	azimuthal angle
A_{throat}	surface area of the throat
c^*	theoretical characteristic velocity of the throat flow rate
P_i	stagnation pressure
r	radial position
t	time
x	axial position
X_e	length of the truncated domain

Subscripts

$\_$	vector
$_i$	imaginary part
$_r$	real part

Superscripts

*	dimensional variable

I. Introduction

Thrust oscillations, due to inflow pressure fluctuations that exist in large solid rocket motors, are observed and studied for several years. They have also been pointed out in reduced scale motors as demonstrated by Prevost[1] . Measurements exhibit frequency paths which characterize the pressure fluctuations. These frequency paths are identified as instabilities. In order to understand the origin of such instabilities a pioneer study, by G. Casalis *et al*[2] , involving a hydrodynamic stability analysis, has demonstrated the key role played by the parietal vortex shedding (PVS). However, this first attempt, based on a small perturbation technique and assuming a wave-like form for the perturbation, leads to a non-consistent approach. Thanks to recent developments[3] , hydrodynamic stability calculations have been done with a consistent approach, called the biglobal approach. Instead of assuming the perturbation as an one dimensional wave-like mode, the perturbation is searched with a more general form. A rather complete description of this approach has been previously given[4] . Works performed by Theofilis *et al*[5,6] have previously proved the pertinence of the

*PhD student, Department Models for Aerodynamics and Energetics, Member AIAA.

†Research Engineer, Department Models for Aerodynamics and Energetics, Member AIAA.

biglobal approach using it successfully on different non-parallel flows. Other approaches, and in particular the energy-balance method proposed by Flandro and Majdalani[7,8], have been developed in order to model the thrust oscillations. The link between the energy-balance method and the hydrodynamic stability is not fully understood yet, but matching the two approaches may result in a new way of characterizing the influence of the acoustic modes in solid rocket motors.
From the results exhibited by the biglobal approach, comparisons with experimental results have been carried out. The goal of this paper is to present a detailed analysis of the comparisons, in order to provide an accurate description of the thrust oscillations phenomenon. Special emphasis will be given on the role of some geometrical characteristics of the motors upon the amplitude of the pressure fluctuations.
Thus, the paper is organized as follows. The first section is dedicated to the main results issued from the biglobal stability calculations. Then, the experimental set-ups and corresponding firings will be described. After some comments on the comparison procedure, we will focus on the different comparisons between the theoretical results and the experimental ones. Finally, a detailed analysis of the measured frequency paths is given.

II. Results of the biglobal linear stability calculations

This paper is not dedicated to the biglobal linear stability theory itself. This later is detailed in a recently published paper[3] and first comparisons with solid propellant motors[4] already proved the pertinence of this approach. Thus only the main points of the theory will be recalled in the following.
The biglobal linear stability analysis is based on a small perturbation technique. It means that a small perturbation of an initially fixed mean flow is searched. The considered mean flow is the well-known Taylor-Culick flow[9,3], that models a laminar axisymmetric flow inside a purely cylindrical solid rocket motor. This flow depends on two parameters : the radius R and the injection velocity V_{inj}. Using these two parameters, it is easy to define dimensionless variables $\underline{x} = \dfrac{x^*}{R}$ ($\underline{x}$ stands for the position vector in cylindrical coordinates (x, r, θ)) and $\underline{u} = \frac{u^*}{V_{inj}}$ ($\underline{u}$ stands for the velocity vector (u_x, u_r, u_θ)). As this mean flow is non parallel (the mean velocity depends strongly on x and r), the perturbation $\hat{q}$ is assumed to be axisymmetric and can be written with the following form :

$$\hat{q} = q(x, r) \exp(-i\omega t) \quad \omega \in \mathbb{C} \tag{1}$$

This modal form is superimposed to the mean flow and injected into the Navier-Stokes equations written for an incompressible one-phase fluid. The only remaining parameter of the obtained system of equations is the Reynolds number $Re = \dfrac{RV_{inj}}{\nu}$. After linearization, the system is discretized on a domain $(x, r) \in [0, X_e] \times [0, 1]$, leading to a generalized eigenvalue problem :

$$\underline{\underline{\mathcal{A}}}\ \underline{X} = \omega\ \underline{\underline{\mathcal{B}}}\ \underline{X} \tag{2}$$

where $\underline{\underline{\mathcal{A}}}$ and $\underline{\underline{\mathcal{B}}}$ are matrices corresponding to the used discretization method. For a given value of the Reynolds number Re, solving the stability problem means finding all the eigenvalues ω, each one being associated with an eigenvector $\underline{X}$ which stands for an arrangement of the discretized values of the spatial perturbation field $q(x, r)$. From the previous published papers[3,4], one can sum up the results into five main conclusions :

- the whole set of eigenvalues ω, called spectrum, is discrete
- all the eigenvalues ω have a negative imaginary part ω_i
- for ω_r sufficiently large [a], all the eigenfunctions $q(x, r)$ are exponentially amplified in the streamwise direction x
- the results weakly depend on the Reynolds number Re
- ω_r does not depend on the length X_e but ω_i does

[a] In practice we can consider that the lower limit value is $\omega_r = 30$

The first and second points imply that there exists only a discrete set of circular frequencies ω_r which are able to emerge in the mean flow and that these circular frequencies stand for temporally stable modes, ω_i being the temporal growth rate of the modal form (1). But the third point conversely claims that each mode (ω_r being sufficiently large) is exponentially amplified in the streamwise direction x. Thus there is a competition between the temporal decrease and the spatial amplification. Finally, the last two points give some information about the influence of Re and X_e. In particular, we can consider that X_e is a passive parameter for the circular frequencies ω_r but it rules the temporal damping : the larger X_e, the smaller $|\omega_i|$.

III. Detailed analysis of the measurements

A. Set-ups description

The set-ups presented in this paper belong to three families called LP9, LP10 and LP6. An accurate description has been given by Prevost[10] . These set-ups are subscale motors of the P230 booster of the European launcher Ariane 5, working with solid propellant. It means that they have an aspect ratio of the same order of the P230 one. They are equipped with pressure sensors at the head-end and near the throat. From these signals, we can have access thus to the time evolution of the pressure fluctuations in the two locations.
Each set-up of the three families corresponds to a specific firing, different firings have been carried out. One can identified a firing by its number β and the name of its family LPα. Thus, in all the following, a firing will be written as LPαtβ ("t" stands for the French translation of firing : "tir").
Let us begin with the simplest motor : LP9. All the firings belonging to the LP9 family have a cylindrical load, meaning that each propellant grain is purely cylindrical. The LP9t10 is made of a single propellant grain. One can expect that at each time the mean flow generated by the combustion of the propellant grain will be close to the Taylor-Culick one, and so the LP9t10 will stand for the reference. Starting from the LP9t10 we increase the complexity of the load by introducing, one by one, some modifications that exist in actual solid rocket motors. Table 1 presents the different firings with their modifications compared to the reference LP9t10. In addition to this table, figure 1 provides sketches of the different firings analyzed in this paper. The successive modifications, mentioned in table 1, are the following ones : the presence of an intersegment (inter.) between the two main propellant grains, the existence of a head-end cavity (head. cav.), a modification of the aspect ratio (asp. ratio) of the motor, an increase of the throat diameter (throat D), the arising of an aft-end cavity (aft. cav.) once the propellant is burned in the recess zone at the aft-end, the tapered (tap.) shape of the propellant grains and finally a scale effect (scale). Thus, we will move on from the simple case of firing LP9t10 to firing LP6t27 whose configuration is very close to the P230 one (except the scale).

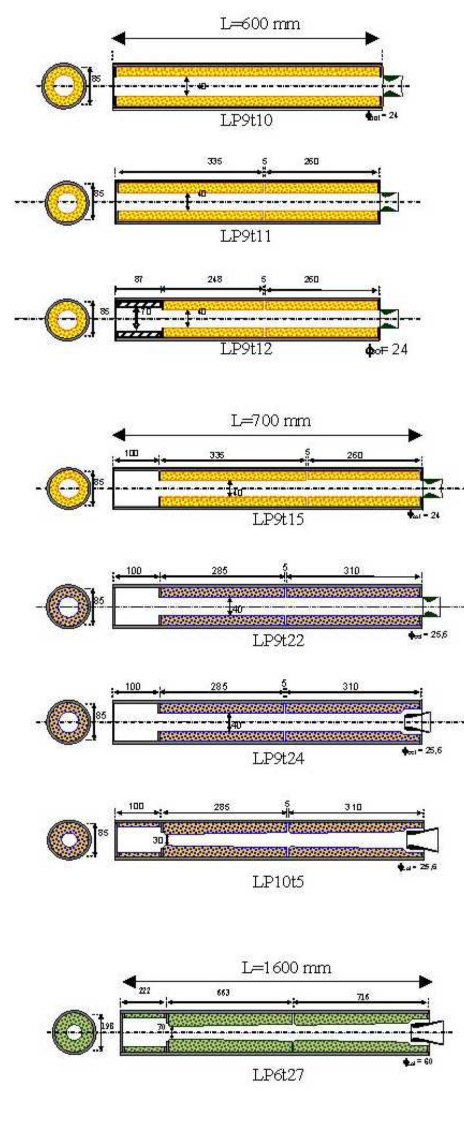

Figure 1. Sketches of the different firings LPαtβ

B. Measurements analysis

1. General purpose

As mentioned before, we have access to two pressure signals. The pressure fluctuations are responsible of the thrust oscillations.

	inter.	head. cav	asp. ratio	throat D	aft. cav	tap.	scale
LP9t10							
LP9t11	×						
LP9t12	×	×					
LP9t15	×	×	×				
LP9t22	×	×	×	×			
LP9t24	×	×	×	×	×		
LP10t5	×	×	×	×	×	×	
LP6t27	×	×	×	×	×	×	×

Table 1. Presence or not of influential elements in the firings LPαtβ.

The main characteristic of their time evolution is the existence of frequency paths. As it is a time-frequency phenomenon it is necessary to use a Short-Time Fourier Transform (STFT) in order to get the time evolution of the pressure fluctuations frequencies. With proper parameters (such as the number of points used for the Fourier transform), one gets a frequency resolution less than 2 Hz and a time resolution around 0.02 s for LP9 and LP10 firings. Before dealing with all the results of the different STFT performed, it is important to note that there is no major difference between the results of the STFT coming from the head-end pressure signal and from the one located near the throat. In both cases, the results exhibit exactly the same frequency paths. But, the results of the aft-end pressure signal are more "noisy". It means that there is more amplitude on all the frequencies, especially during the first part of the firing. This can be partly explained by the existence of a turbulent zone in the downstream part of the motor. In cold gaz facilities[11,12] , it has been shown that the transition to turbulence occurs at a location which corresponds to a more or less constant dimensionless value : $x_T = x_T^*/R = c^{te}$. If one extrapolates this result to live motor, one can see that, as R increases, the turbulent zone will be pushed forward during the firing. Thus, at the beginning of the firing the turbulent zone is spread over a large region of the motor and then this zone is continuously diminishing. This could explain the observed "noise" on the aft-end pressure signal at the beginning of the firing. But, as far as the authors know, there is no evidence of such a behavior in a real motor. Even if it looks like a reasonable explanation, it has to be confirmed.

Now, as there is no difference between the frequency paths exhibited by the pressure signals at the head-end and at the aft-end, one performed all the STFT for all the firings on the head-end pressure signals. The results are reported in figures 2(a) and 2(b). They show the results of the different STFT by plotting iso-contours of amplitudes in the time-frequency plane. For the sake of clarity, the amplitudes are normalized using the infinity norm. So, the maximum amplitude reached in each subfigure is equal to unity. When the frequency path phenomenon is very amplified it is isolated from the rest and appears almost alone. Conversely, when there is a low average level of amplitude, the contours are spread over a large part of the figure, as it the case for firing LP9t10 and LP9t11.

For years, the acoustic modes are believed to play an important role in the merging of the frequency paths. The main reason is that the frequency paths are always located around the different acoustic modes of the motors. Thus, each subfigure presents the STFT results of the considered firing around the first acoustic mode, where the maximum amplitude level is reached. There are also some frequency paths arising around the second and third acoustic modes but usually with less amplitude. For higher acoustic modes, the energy is so weak that is hard to say that there also exists some frequency paths.

2. LP9t10

The first analyzed case is the simple configuration of firing LP9t10. The measured frequencies show no particular organization. There is no explicit frequency paths. However it has to be remained that the pressure fluctuation average amplitude is very low.

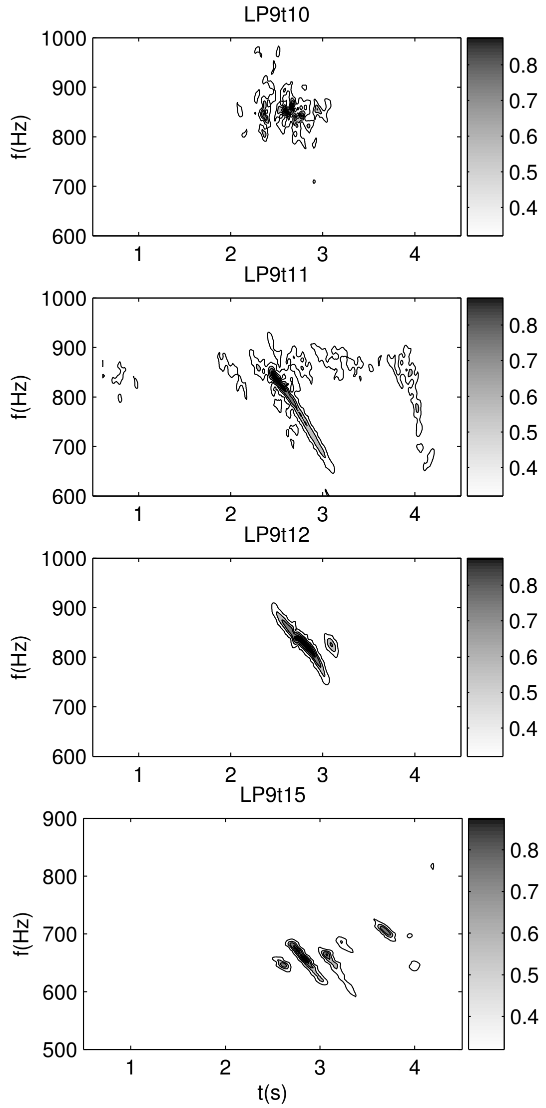

(a) Firings LP9t10, LP9t11, LP9t12 and LP9t15

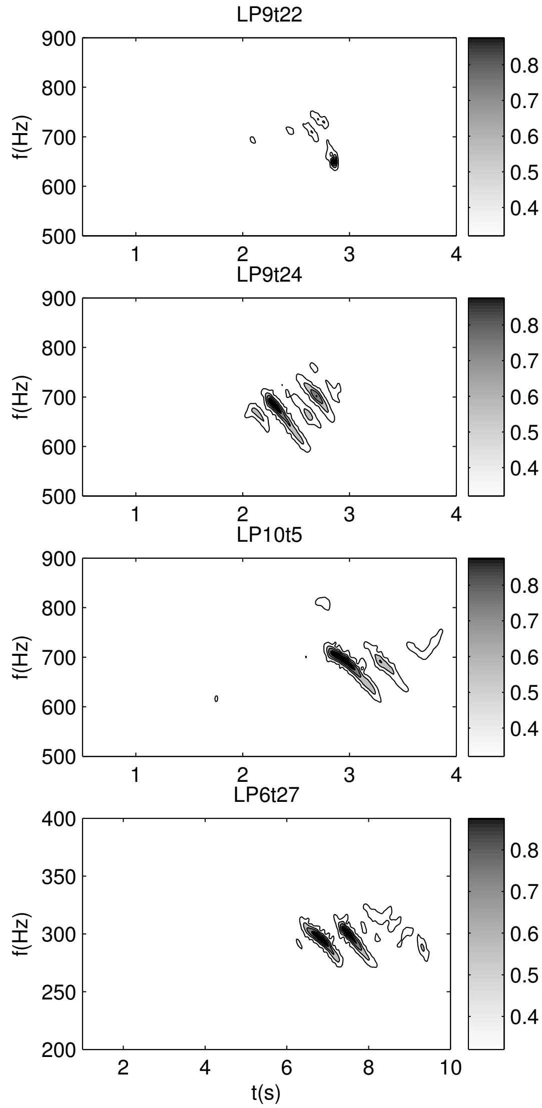

(b) Firings LP9t22, LP9t24, LP10t5 and LP6t27

Figure 2. STFT of all the analyzed firings. The measured pressure fluctuations are represented by iso-value contours.

3. LP9t11

It has been shown by Prevost *et al.*[10] that the presence of an intersegment between the propellant grains increases the level of the fluctuations. In fact, the STFT of the pressure signal of firing LP9t11 exhibits a frequency organization. One can clearly see a long frequency path surrounded by short ones.

4. LP9t12

Then a head-end cavity is added, what makes the fluctuations amplitude increase. The results for firing LP9t12 exhibit two frequency paths. Once again one of them is more important.

5. LP9t15

For the first three firings the average frequency around which the frequency paths occur is about 850 Hz. When changing the aspect ratio of the motor, see LP9t15 firing results, this average frequency moves about 700 Hz. In all cases, calculations show that this average frequency corresponds to the first longitudinal acoustic mode. And so, increasing the motor length by changing the aspect ratio, makes this frequency decrease as it is observed in the experiments. One can also note that the amplitudes of the fluctuations are increased for firing LP9t15, resulting in the merging of several explicit frequency paths. Moreover, it has to be pointed out that some frequency paths can coexist. At a given time, several frequency paths are observed.

6. LP9t22

The next analyzed firing is the LP9t22 one. Here, the increase of the throat diameter implies a drop of the total pressure all along the motor. The main consequence of this modification is the occurrence of paths with a lower amplification level. However, some frequency paths can be observed.

7. LP9t24

To conclude the analysis of firings having cylindrical propellant grains, the LP9t24 is analyzed. In addition to all the previously presented modifications, an aft-end cavity is added. This cavity is not really added from the very beginning of the firing, but is a consequence of the burning of the last part of the downstream propellant grain. Because of the integrated nozzle, the propellant grain must have a recess, and thus this part will be rapidly burned. Thus, an aft-end cavity appears. In the LP9t24 case, this arises at $t = 2\ s$. On figure 2(b), one can see that at this time a short particular frequency path occurs. After, some frequency paths are observed.

8. LP10t5

The last two cases are firings LP10t5 and LP6t27 for which tapered propellant grains are used. Apart from the end of firing LP10t5, where a special shape for the last frequency path is observed, there is no significant difference compared to the previous cases. This shape is due to the so-called hump effect, which implies an increase of the combustion velocity when the thickness of the propellant grain is very thin. For conical propellant grain this arises during a relatively long time at the end of the firing, because of the regression of the propellant grains. One can observe this phenomenon for all firings which have conical grains[10] .

9. LP6t27

Finally, the last presented firing LP6t27, enables us to give a general conclusion on scale effects. All the quantities have been proportionally increased. In particular, the amplified frequency range has been modified. But the results exhibit the same frequential behavior. Apart from a pure scale effect, there is no significant modification induced.

IV. Comparisons theory-experiments

A. Equivalent Taylor-Culick flow construction

Before explaining how the comparisons are performed, we have to face the problem of unsteadiness. Because of the combustion process which makes the geometry of the propellant grains evolve during the firing, the flow inside a LPαtβ firing is unsteady. However, the characteristic frequency of the time evolution of the flow is low compared to the pressure fluctuations one[3] . Consequently, the perturbations are assumed to be independent of the flow unsteadiness. At each time, the pressure fluctuations are generated by a flow which can be assumed steady.

Now that we have presented the measurements of the different firings, the idea is to compare them to the theoretical results. But the main difficulty is that the mean flow used by the linear stability code is restricted (up to now) to the analytical Taylor-Culick flow. So, it is necessary to build an Equivalent Taylor-Culick Flow (ETF). We have thus to determine the only two parameters of such a flow : R and V_{inj}, whose values are independent of x. Generally speaking, a LPαtβ does not satisfy these requirements. This stage, called

construction of an ETF, is the core of this section. Once known the parameters R and V_{inj}, it will be possible to turn the dimensionless theoretical results into dimensional ones.
As the flow is assumed steady, we only need to have access to the two parameters R and V_{inj} of the mean flow at each time. Except in the LP9t10 case, the flow inside a motor is different from the one generated by fixed values of a radius and an injection velocity. To construct the ETF, we use the results of a 1D regression code called PERSE. It has been developed by J.C. Godon at ONERA Le Fauga-Mauzac. Using the initial geometry and the propellant properties, this code provides the time evolution of thermodynamical quantities during a firing. Thanks to the different given values, it is possible to build a radius R and an injection velocity V_{inj}. We will now describe the procedure.

1. *Radius R*

For the simple case of firing LP9t10, it is obviously easy to build R. In fact, the PERSE code provides the diameter of the flow for each x, noted $D_{perse}(x)$, which is a constant value all along the motor. But, generally speaking R is a function of x. So it is necessary to perform a spatial average along the burning length L :

$$R = \frac{1}{L}\int_0^L \frac{D_{perse}(x)}{2}dx \tag{3}$$

For conical propellant grains, the angle being small, it appears reasonable to use (3) and to reduce the effect of tapered grains to the injection velocity (increasing the radius makes the flow slows down which implies a decrease of the injection velocity). If there is an intersegment, as in the LP9t11, there is a part without propellant, the size of which increases during the firing (the propellant burns from its lateral faces). However, this part remains short compared to the length of the propellant grains. To take this into account, we use formula (3) on each propellant grain. It is also possible that there exists a head-end cavity. Its presence will affect the injection velocity of the ETF because of the induced total pressure drop. But its effect does not have to be integrated into the radius of an ETF. The same is true for aft-end cavities. Finally, the construction of R is easy and is based on a spatial average along the burning surfaces (3).

2. *Injection velocity V_{inj}*

Contrary to the construction of the radius R, getting a relevant injection velocity is delicate. There are many ways of calculating an injection velocity. Let's consider two examples. The PERSE code provides the combustion velocity V_c at different locations x. The local injection velocity is then deduced from it using the mass conservation : $\rho_{propellant}V_c = \rho_{gaz}V_{inj}$. But if one considers this injection velocity, one forgets the flow rate injected by intersegments. Thus, the ETF would have a lower flow rate than the considered flow (given by the PERSE code). This first example leads us to the second one which basic idea is the conservation of the flow rate. The PERSE code estimates the flow rate at the throat by :

$$Q_{throat} = \frac{P_i A_{throat}}{c^*} \tag{4}$$

One can then deduce the injection velocity of an ETF thanks to this flow rate :

$$V_{inj} = \frac{Q_{throat}}{2\pi\rho RL} \tag{5}$$

with R and L the radius and the length of the ETF described above. Thus, we have built an ETF that conserves the flow rate at a given distance L. But, the theoretical circular frequencies ω_r coming from the stability theory are not depending on the length on which the calculation is performed. The notion of flow rate at a distance L is not relevant for the Taylor-Culick flow. The important point is the spatial evolution of the flow rate, because it is linked to the injection velocity. The flow rate of the Taylor-Culick flow passing through a section $x = c^{te}$ is a linear function of x. The slope is directly linked to the injection velocity. This leads to the final choice for the calculation of the ETF injection velocity. The PERSE code gives the surfacic flow rate at different locations x. From these values, one estimates the injection velocity thanks to :

$$\pi R^2 Q_{perse}(x) = 2\pi R\rho V_{inj}x \tag{6}$$

More precisely, we calculate the slope Q_{perse}/x of the flow rate along each burning surface and take the average value. The ETF injection velocity is deduced from it using (6).

In the LP9t10 case the three ways of calculating the injection velocity give the same results. But for more complicated geometries, only the third way based on the slope of the flow rate answers the requirements of an ETF. The authors want to insist on the fact that this is not the unique way of finding the injection velocity of an ETF.

B. Comparisons

1. *Frequency paths*

Finally, at each value of the time during the firing, we have built an ETF by determining a radius $R(t)$ and an injection velocity $V_{inj}(t)$. Any LPαtβ has its own ETF, and we only have to perform the stability calculation for each Reynolds number Re corresponding to each ETF. The problem is that the Reynolds number is based on R and V_{inj} which are functions of the time. But the range in which the Reynolds number evolves during each firing is sufficiently small so that we can consider that the stability results are not significantly influenced by the evolution of Re, see section II. We just have to perform a unique calculation for an average value of the Reynolds number. Moreover, it appears that the different ranges of Reynolds numbers for all the firings are more or less identical. Thus we perform only one stability calculation at $Re = 6500$ and use the results for all firings. Some circular frequencies (those which are reported in figures 3(a) and 3(b)) are given in table 2.

49.007	53.273	57.920	63.072	68.911	75.710	83.504	94.518	108.210

Table 2. Values of the circular frequencies ω_r used for the comparisons, $Re = 6500$

Once known, the circular frequencies are turned into dimensional frequencies with the use of the following formula :

$$f(t) = \frac{V_{inj}(t)}{2\pi R(t)}\omega_r \tag{7}$$

with $R(t)$ and $V_{inj}(t)$ determined by (3) and (6). For a given stability mode ω_r one obtains a time evolution for its corresponding frequency. Thus, a discrete set of circular frequencies provides a modes network. Each mode of this network has a frequency which evolves during the firing, as frequency paths do.
On figures 3(a) and 3(b), the networks are drawn as dashed lines. The comparisons show a very good agreement. It has to be reminded that the theoretical network is calculated independently of the measurements.

2. *Amplitudes*

Up to now, the comparisons concerned frequencies, the theoretical circular frequencies ω_r were compared to the measurements. It remains to compare the temporal growth rate ω_i. As the frequency paths arise around the longitudinal acoustic modes of the motor, filtering the pressure signal around the first acoustic mode, allows to compare the measured decrease with the predicted one. For example, we focus on the LP9t15 and LP9t24 firings which exhibit isolated frequency paths. In fact, in order to make relevant comparisons the modes have to be isolated, so that the measured decrease is associated with a unique mode. The main difficulty is that the dimensionless length X_e of the motors is changing during the decrease phase. As written above, see section II, ω_i is depending on X_e. However, for each mode, one can consider an average value for X_e as the range in which it evolves is very small. Once the calculation is made with the chosen values of X_e and Re, the dimensional temporal decrease of the amplitude A is evaluated thanks to the following formula :

$$A = A_0 exp\left(\int_{t_{init}}^{t} \frac{V_{inj}(u)}{R(u)}\omega_i du\right) \tag{8}$$

where t_{init} is the initial time at which the decrease starts and A_0 a constant standing for the initial amplitude (for linear problems, the amplitude A is always function of an initial constant A_0). The results are

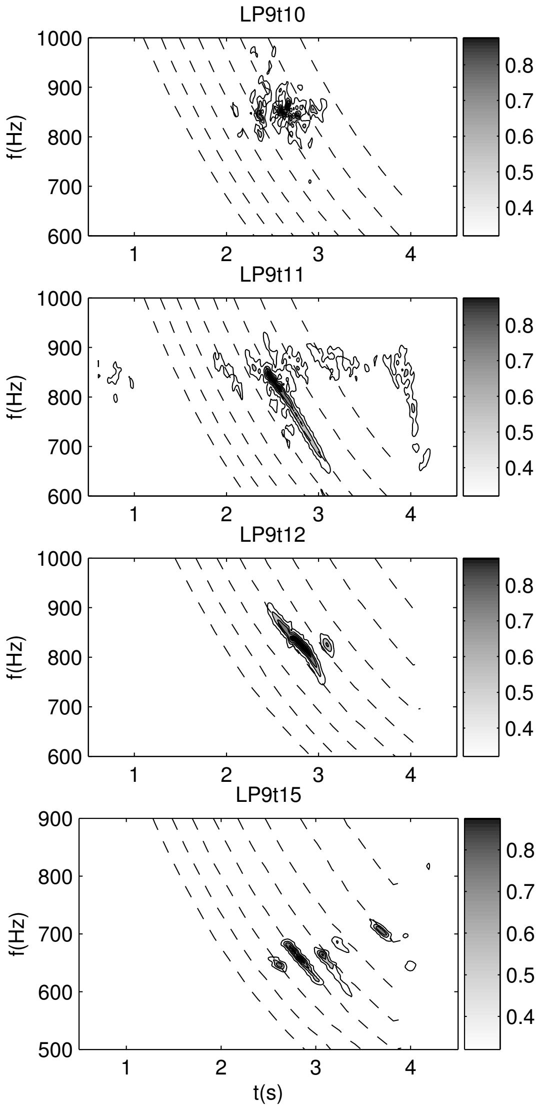

(a) Firings LP9t10, LP9t11, LP9t12 and LP9t15

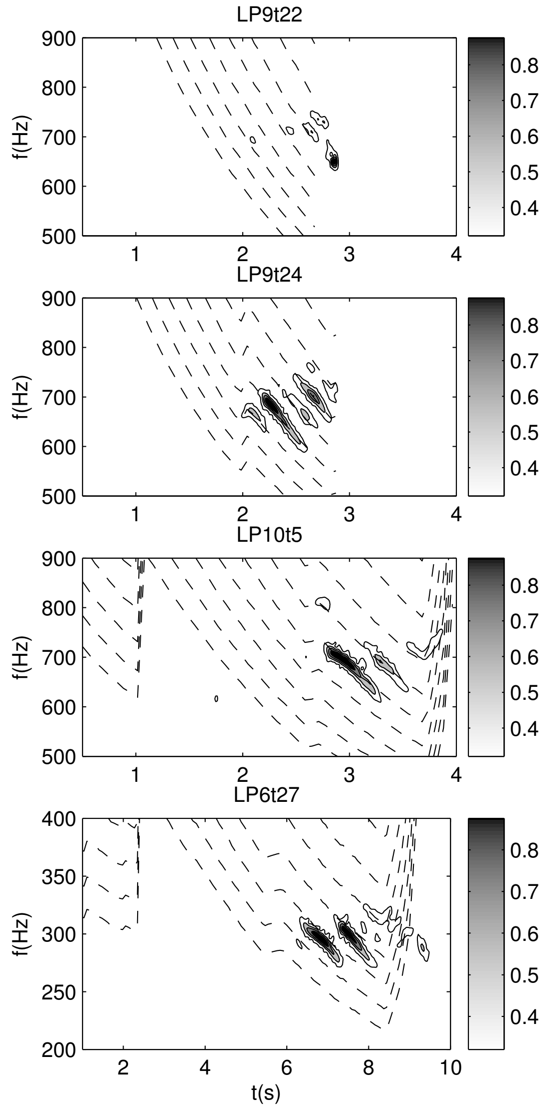

(b) Firings LP9t22, LP9t24, LP10t5 and LP6t27

Figure 3. STFT of all the analyzed firings. The time evolutions of the theoretical modes are drawn as dashed lines, whereas the measured pressure fluctuations are represented by iso-value contours.

shown on figures 4(a) and 4(b). Once again the agreement is very good. However it has to be moderated. The values of X_e when the frequency paths arise are all greater than 15. We have already assumed, by extrapolating cold-gas results[11,12] , that the transition is located at $x_T = c^{te}$. This value x_T is around 12 in cold-gas facilities. Even if extrapolating the cold-gas results to live motors is questionable, it seems that for large value of x, in particular greater than 15, the flow may not be laminar but turbulent. If so, the linear stability theory can not be applied for such large values of X_e, the main flow being different from the Taylor-Culick one. Finally, it is not pertinent to give credit to the good obtained agreement in terms of values. Nevertheless, the measured decreases exhibit clearly an exponential evolution which is coherent with the theory. It has to be noticed that all the restrictions concerning X_e and the calculation of ω_i do not exist for the calculation of ω_r.

From all these comparisons, in terms of frequencies (ω_r) and in terms of temporal damping (ω_i), we propose an interpretation of the thrust oscillations occurrence.

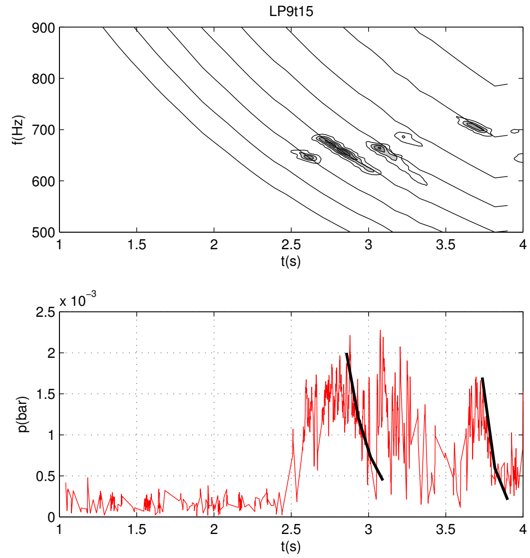

(a) Firing LP9t15

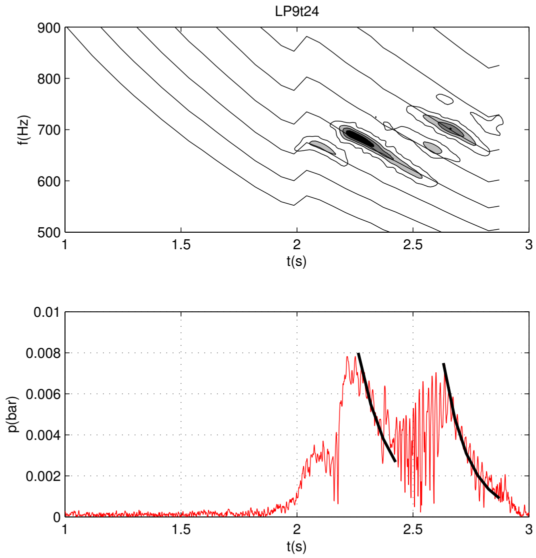

(b) Firing LP9t24

Figure 4. Comparisons of the measured decrease of frequency paths with stability theory predictions.

C. Interpretation

The theoretical networks match the measurements 3(a), 3(b). It means that in all the analyzed firings the frequency paths result from the same phenomenon. The presented linear stability theory shows that this phenomenon is the merging of intrinsic instabilities. The flow generated by the combustion of a propellant grain generates its own instabilities. So, the observed frequency paths, in all the firings, hold their origin in the primary configuration of firing LP9t10. However, the low level of amplitude reached in this case makes it hard to see explicit frequency paths.

For firings LP9t11 and LP9t12, the measurements exhibit a long frequency path. In both cases, the presence of an intersegment may be at the origin of this behaviour. Because of that, the theoretical networks do not match exactly these particular frequency paths. In fact, as the propellant grains burn from its lateral faces, the intersegment size increases and so the frequency associated with the induced vortex shedding does not have to follow the ratio V_{inj}/R. However, these firings also exhibit short frequency paths which evolutions are in agreement with the predictions.

For firings LP9t15 and LP9t22, the coexistence of several frequency paths give credits to the biglobal approach results which provide a set of circular frequencies. Thus, the observed frequency paths can not be due to a unique mode which would have jumped from a path to an other one.

The LP9t24 firing is interesting because of the merging of its aft-end cavity. As mentioned before, this implies the occurrence of a special frequency path with a singular shape. When the recess zone is fully burned, there is a small pressure drop. Thus, the calculated ETF injection velocity V_{inj} increases at this time, around $t = 2\ s$. Consequently, the theoretical network takes into account the merging of the aft-end cavity and matches perfectly the evolution of the frequency paths. The measured frequency paths follow exactly the evolution of the ratio V_{inj}/R as long as they are linked to intrinsic instabilities (and not to an intersegment).

Finally, the last two cases LP10t5 and LP6t27 confirm the proposed interpretation. However, one can note a bad prediction near the end of the firings. As explained before, at the end of the firing the hump effect makes the injection velocity increase. Unfortunately, the PERSE code is unable to provide the precise increase of the injection velocity. Thus, the theoretical network is not following the measurements at the end of these firings. Nevertheless, the time at which this increase arises is well predicted.

The main interpretation resulting from these comparisons 3(a) 3(b) is that in all the firings the observed frequency paths are the occurrence of intrinsic instabilities. These instabilities are well predicted by the biglobal approach.

Even if the comparisons give a good agreement, some points remain unclear. On one hand, the theoretical modes are temporally stable but are exponentially growing in the streamwise direction x. Thus, they need to be excited in order to merge. On the other hand, the experiments show frequency paths arising around the acoustic modes, and in particular around the first one. It seems reasonable to believe in an interaction between the intrinsic instabilities of the flow and the acoustic modes. When a theoretical mode comes close to an acoustic mode (actually, the first one in figures 3(a) and 3(b)) it is amplified. Then its time evolution moves its frequency away from the acoustic one. But, during that time the following mode has arrived in the vicinity of the acoustic mode. Consequently, a frequency paths phenomenon is observed, which explains the possible coexistence of several modes.

Once the modes have been amplified, they have to decrease exponentially, as claimed by the linear stability analysis. Figures 4(a) and 4(b) show that the measurements follow the predictions. These good agreements confirm the possible interaction between the acoustic modes and the theoretical ones. Future developments may bring new elements concerning this possible interaction.

To conclude the interpretation of the thrust oscillations phenomenon, a last point has to be analyzed. On one hand, the measurements come from the head-end pressure signal. On the other hand, the stability modes are exponentially growing in the streamwise direction x and so they have a negligible amplitude at the head-end. The resulting question of these two conflicting informations is to know what is really measured at the head-end. It is well-known that a fluctuation passing through a sonic throat emits a reflected pressure wave which conserves the fluctuation frequency. Consequently, the frequency paths measured at the head-end are the traces of the amplified stability modes which have passed through the throat.

V. Summary

In the present paper, a series of subscale motors measurements has been investigated. From the simple configuration of firing LP9t10 to the P230-like configuration of firing LP6t27, all the motors exhibit the same phenomenon characterized by frequency paths. Thus, the existence of intrinsic instabilities of the main flow has been pointed out. A confirmation is given by the linear stability theory. In fact, the results of this approach provide a discrete set of circular frequencies ω_r. In order to make the comparisons with the experiments, it has been necessary to build the radius R and the injection velocity V_{inj} of an equivalent Taylor-Culick flow (ETF). Once the set of ω_r has been turned into dimensional frequencies, the comparisons give a very good agreement in all cases. Moreover, some little differences, for example for firing LP9t11, show the role of the intersegment. Now that the frequency paths have been identified as intrinsic instabilities of the main flow, it remains to explain their merging. The linear stability results provide information, such as the temporally stable nature of the stability modes, which help to understand the global mechanism of the thrust oscillations. The measurements show that the frequency paths arise around the acoustic modes. Thus, a coupling mechanism is believed to exist between these acoustic modes and the stability ones. After they have been amplified, the modes are exponentially decreasing. Consequently, the frequency path phenomenon appears to be a succession of modes, amplified and then decreasing. In this analysis, the acoustic modes are only exciting sources for stability modes, they are not at the core of the thrust oscillations.

Acknowledgments

This study has been supported by the French Space Agency CNES and by ONERA. The authors thank M. Prevost and J-C. Godon from ONERA Le Fauga-Mauzac for their accurate measurements, their help and their relevant advices.

References

[1]Prevost, M., Godon, J. C., Maunoury, J., and Entrialgo, E., "On the representativity of small scale motor tests. Instabilities in solid rocket motors," *Transports aeriens et techniques spatiales*, Colloque franco-vietnamien Hano, Vit Nam, 21-22 novembre 2002.

[2]Casalis, G., Avalon, G., and Pineau, J. P., "Spatial instability of planar channel flow with fluid injection through porous walls," *Physics of Fluid*, Vol. 10, No. 10, October 1998.

[3] Chedevergne, F., Casalis, G., and Feraille, T., "Biglobal linear stability analysis of the flow induced by wall injection," *Physics of Fluids*, Vol. 18, January 2006.

[4] Chedevergne, F. and Casalis, G., "Thrust Oscillations in Reduced Scale Solid Rocket Motors, part I : a Theoretical Approach," *41st AIAA/ASME/SAE/ASEE Joint Propulsion Conference and Exhibit*, Tucson, Arizona, 10-13 July 2005.

[5] Theofilis, V., "Advances in global linear instability analysis of nonparallel and three-dimensional flows," *Progress in Aerospace Sciences*, Vol. 39, 2003, pp. 249–315.

[6] Theofilis, V., Fedorov, A., Obrist, D., and Dallmann, U. C., "The extended Görtler-Hämmerlin model for linear instability of three-dimensional incompressible swept attachment-line boundary layer flow," *Journal of Fluids Mechanics*, Vol. 487, 2003, pp. 271–313.

[7] Flandro, G. A. and Majdalani, J., "Aeroacoustic Instability in Rockets," *AIAA Journal*, Vol. 41, No. 3, March 2003, pp. 485–497.

[8] Majdalani, J., Flandro, G., and Fishbach, S., "Some rotational corrections to the acoustic energy equation in injection-driven enclosures," *Physics of Fluids*, Vol. 17, No. 7, July 2005, pp. 074/02–1–074/02–20.

[9] Taylor, G. I., "Fluid flow in regions bounded by porous surfaces," *Proc. of the Royal Soc. Series A, London*, Vol. 234, No. 1199, 1956, pp. 456–475.

[10] Prevost, M. and Godon, J.-C., "Thrust Oscillations in Reduced Scale Solid Rocket Motors, part I : Experimental Investigations," *41st AIAA/ASME/SAE/ASEE Joint Propulsion Conference and Exhibit*, Tucson, Arizona, 10-13 July 2005.

[11] Yagodkin, V., "Use of channels with porous walls for studying flows which occur during combustion of solid propellants," 18th International Astronautical Congress AGARD, 1967.

[12] Avalon, G. and Lambert, D., "Campagne d'essais VALDO, periode 2000/2001," Tech. Rep. RT 2/05424 DEFA, ONERA, Etablissement de Palaiseau, octobre 2001.